Surface distribution of phenol photodegradation in Rotating Disc Reactors

By Ewan Westgate, Dominic Johnson and Farid Aiouache*
Lancaster university, School of engineering, LA14YR. Lancaster, UK

*Corresponding author: Farid Aiouache, e-mail: f.aiouache@lancaster.ac.uk

Keywords: Photocatalysis, Rotating Disc Reactor, Phenol Degradation, TiO_2, 3D modelling simulation

Abstract
Photocatalytic rotating disc reactors offer enhanced illuminated surface area but are constrained by thin reactive films, laminar flow, mass-transfer limitations, and limited throughput. This study investigates these limitations and proposes a hydrodynamic approach to improve reactor performance while providing insights relevant to future scale-up. A three-dimensional CFD model based on the level-set method, coupled with ray tracing, was developed to simulate two-phase air–water flow and incorporate surface reaction kinetics. Simulations were validated against laboratory experiments using a custom-fabricated TiO_2-coated rotating disc reactor. Surface modification via sandblasting increased micro-roughness, improving coating adhesion, while dip coating produced uniform catalyst films with reproducible linear growth upon successive deposition. Hydrodynamic analysis revealed radially non-uniform performance, with increasing tangential velocity and shear towards the disc periphery enhancing mass transfer and catalytic activity. Phenol conversion increased from 8.71% at 60 rpm to 11.42% at 240 rpm, and further reducing liquid immersion improved conversion to 17.42%. The achieved photocatalytic space–time yield reached 93.6 mmol day^{-1} kW^{-1} and was primarily limited by mass transfer. These results highlight the importance of hydrodynamic control in improving photocatalytic efficiency and provide guidance for the future development and scale-up of rotating disc reactors.

1. Introduction

Photocatalysis is transforming modern catalysts across various applications, such as water treatment, removal of trace materials, self-cleaning, anti-fogging, and cancer treatment.[1] Upon optical irradiation of their conduction band, the electrons undergo reactions with electron-donating or electron-accepting species adsorbed on the photocatalyst surface via electron transfer. Reactive oxidation species (e.g., hydroxyl and peroxyl radicals) with short lifetimes are formed, which can irreversibly break down and mineralise the species involved in photocatalytic reactions [2,3]. In the context of photocatalytic degradation of pollutants in water, the irreversible oxidation of organic compounds produces carbon dioxide and water. [3] Titanium dioxide (TiO_2), the most well-known photocatalyst, is typically suspended in a slurry or immobilised on the surface support in a reactor, preventing the need for catalyst removal after the reaction [4]. TiO_2 activation occurs at wavelengths below 380 nm for anatase and 400 nm for rutile, two common forms of TiO_2 [5].

This technology is gaining attention because of its potential for scale-up and efficient utilisation of illuminated surface area. Engineering efforts are advancing towards a variety of industrial applications by addressing the challenge of the optical path's penetration through the liquid medium, which is caused by photon absorption. [4]. The mitigation of the reduction in incident intensity on the photocatalyst surface consists of implementing thin films generated by reactive flow in rotating disc reactors (RDRs) that are partially submerged in the reaction mixture, mounted on horizontal shafts, and coated with immobilised TiO_2.[6, 7] Whilst rotating, the disc drags up a film of liquid from the

reaction mixture onto its surface and the immobilised TiO_2 photocatalyst layer. Disc rotation and thin-film hydrodynamics continuously renew the liquid–solid interface, enhancing mass transfer and reactant availability at the photocatalyst surface. Under these conditions, UV irradiation benefits from hydrodynamic surface renewal, ensuring repeated exposure of fresh reactants to the illuminated catalytic surface, promoting effective photon utilisation and reducing mass-transfer limitations on reactive species [8]. Primarily used for viscous and biological fluids, such as in polymer evaporators and bio-nitrification contactors, the RDRs are available in various configurations, including single or multiple discs that co-rotate, counter-rotate or cross-rotate, as well as rotating drum reactors and spinning disc reactors [9, 10]. The behaviour of the surface film and its renewal in non-Newtonian fluids were particularly investigated for viscous fluids. The RDR inherently generates thin liquid films due to centrifugal forces and surface shear. In photocatalytic applications, which typically involve low-viscosity aqueous solutions, these hydrodynamic conditions promote the formation of particularly thin films, thereby enhancing mass transfer, surface renewal, and the distribution of illuminated film area without fundamentally altering the underlying flow dynamics. [11, 12] When the discs rotate, the surface film is subject to shear forces of viscous, gravitational, interfacial and inertial nature. These forces drive the liquid to drain preferentially in radial and angular directions while they remain in contact with the disc surface [13,14]. The flow dynamics are primarily limited by the film thickness, which, in turn, is primarily limited by the rotation speed. Other characteristics, such as the surface area-to-volume ratio, roughness, corrugation, and wettability, play a non-negligible role. [15-20]
In practice, the design of RDRs is close to that of the rotating biological contractors (RBCs). Buechler et al. [21] proposed a design based on the immobilisation of TiO_2 on rotating discs, and Dionysiou et al. [22] presented a vertical RDR which was used in continuous operation for the degradation of several phenolic compounds. Since these breakthroughs, there has been substantial progress in both the optimisation of the original designs and surface kinetic analysis, including adapted geometries and numbers of discs, peak UV wavelengths, protocols for photocatalyst doping and immobilisation, and the operation of RDRs [23-25]. This highlights the progress this technology is making, which is quickly advancing towards industrial-scale applications.
The structure of the photocatalytic RDR consists of three main components: a light source, a disc with photocatalyst immobilised on the surface and the reactor where the bulk effluent is circulated. The discs are set at a prescribed distance apart and partially immersed in the bulk effluent, leaving the fraction of the disc not immersed exposed to UV light for the photocatalytic reaction. As the disc rotates, a thin film of liquid is entrained, and the reaction occurs when the liquid is irradiated [26]. Residence times for the thin liquid film typically range from 0.1 to 3.0 seconds, depending on the fluid's physical properties, reactor size, and rotational speed [20], which affect the overall rate of the redox reaction and the formation of intermediates and products [21-23]. This leads to considering a few key characteristics for the successful design of a photocatalytic reactor, such as a high photocatalyst load per unit reactor volume, the ability to deliver uniform UV irradiation to a high fraction of the photocatalyst surface, and high mass-transfer rates between the liquid effluent and the photocatalyst active sites.

Leveraging computational fluid dynamics (CFD) to model flow operations within the RDR offers an advantageous approach that reduces design costs and promotes scalability. The chemical kinetics of the photocatalytic reaction can be integrated with the fluid flow, allowing the incorporation of mechanistic models into macroscale simulations [22]. This approach focused on viscous fluids, where CFD has been extensively used to investigate the hydrodynamics of the bulk fluid, the development of films on the disc surface, and mixing in these systems. The accuracy of the results was found to be significantly influenced by the meshing strategy used to model the moving parts. Techniques such as the sliding mesh methods [23,24], superposition and dynamic mesh methods [25], demonstrated the asymmetric behaviours of the film flow. These methods often faced challenges related to mesh quality and the need for high computational resources and time [25]. A recent method for modelling pump dynamics used the overset meshing to combine stationary and moving parts for two-phase flow

applications. The methods used the Volume of Fluid (VOF) technique as described to estimate the film thickness dynamics based on the shear rates. [26-30]

The distribution of performance on the discs in photocatalytic RDRs is highly non-uniform and varies spatially due to differences in hydrodynamics, light exposure, and mass transfer conditions across the disc surface. Understanding this distribution is crucial for optimising reactor design and operation, as it directly impacts overall photocatalytic efficiency. One of the most significant factors contributing to local performance variation is the radial position on the discs. As the disc rotates, the linear velocity increases from the centre to the periphery, enhancing shear forces and mass transfer towards the edge. This increase leads to higher reaction rates, aiding in the transfer of reactants to the surfaces of the photocatalyst and the removal of products, thereby promoting surface renewal. This process ultimately allows for better regeneration of the catalyst and limits the accumulation of byproducts, such as intermediate radicals or fouling. In the central zone of the discs, the linear rotational speed is lower, resulting in thicker hydrodynamic films, poorer mass transfer, and reduced reaction rates. While the discs rotate, each point on the surface experiences periodic immersion in fluid and exposure to air or light. This variation along the rotation path creates time-dependent fluctuations in photocatalytic activity at each surface point, which is intermittently illuminated, oxygenated, or immersed in the liquid film as it rotates through the light, air, or pollutant exposures.

Although the dynamic nature of this exposure helps maintain some level of uniformity over time, localised activities may still decline depending on disc configuration and operating conditions. Additionally, the uniformity of the catalyst coating on the disc surface also plays a critical role in local performance. Thicker or uneven coatings can lead to reduced light penetration or mass transfer limitations. Furthermore, localised fouling, due to organic intermediates or particulate deposition, may create dead zones on the disc where performance diminishes over time. In this work, a Level Set - based multiphysics approach is applied to analyse the spatial distribution of phenol conversion on immobilised photocatalytic rotating discs. Phenol was selected as a model compound because it is widely used as a benchmark pollutant in photocatalytic water treatment studies due to its environmental relevance, well-established degradation pathways and sensitivity to both photon flux and mass-transfer limitations. A three-dimensional, two-phase flow model is developed in which air and water are treated as interpenetrating media, each satisfying conservation laws of mass and momentum, enabling accurate tracking of the dynamic gas–liquid interface [30,31]. The modelling approach couples transient hydrodynamics and free-surface evolution with UV ray tracing to characterise the spatial irradiation field incident on the rotating discs. A steady-state ray-tracing solution is transformed into a three-dimensional empirical surface-illumination function and integrated with surface reaction kinetics, enabling quantification of local photocatalytic performance. In addition to mechanistic analysis, photocatalytic performance is evaluated using space–time yield metrics to enable benchmarking against similar reactor configurations. This integrated approach aims to establish a comprehensive optical–hydrodynamic–kinetic modelling methodology for rotating-disc photocatalytic reactors and to provide design insights into thin-film stability, catalyst utilisation, and energy-efficient operation.

2. Methods

2.1. Photocatalyst immobilisation

The design of the batch lab-scale reactor included three discs, a reactor tank, an axle with axle stands and UV lights, all operated at standard temperature and atmospheric pressure [32]. The stainless-steel discs were designed using computer-aided design (CAD) and manufactured with a water jet cutter from a 2 mm stainless-steel sheet. They were etched by sandblasting at 10 bar for 20 seconds and no further surface treatment was added. The TiO_2 slurry was prepared by using a concentration

of 10 g/L TiO_2 particles supplied by Thermo Fisher Scientific Inc. (Anastase powder of higher than 99.7 % purity, less than 25 nm particle size, 60-100 m^2/g BET Specific Surface Area), which were homogeneously dispersed through sonication at 180 W for 20 minutes. The resulting dispersion remained sufficiently stable for up to 1 hour, allowing dip coating to be carried out [33]. This method was chosen for its simplicity and established effectiveness to reach a thickness of micrometres in phenol conversion studies. [18]

The dipping rate of the TiO_2 dispersion promotes the thickness of the photocatalyst layer deposited on the discs [34]. A dipping rate of 0.87 mms^{-1} was used that produced thin layers and avoided the formation of thermal cracks [35]. It necessitated repeated dips to achieve a thickness sufficient for the kinetic studies, as illustrated in section 3.2. After each dip coating, the discs were dried and calcined at 300°C and 450°C, successively, at a rate of 5°C per minute in a CARBOLITE GERO furnace, that has been shown to improve the formation of small crystal sizes of the TiO_2 powder and their adhesion to the surfaces of the discs. [36] The surface distribution of the coating was assessed by using a 3D microscope (LEXT OLS5000, Olympus) with a vertical resolution of 10 nm and a lateral resolution of 120 nm.

2.2.Reactor design

The design of the mechanical parts of the RDR was realised by additive manufacturing using 3D printing facilities, as illustrated in Table 1 and shown in the 2D and 3D schematic models of Figs.1. (a) and (b), with more illustrations in Mov1 as supporting information. The reactor tank (300 x 200 mm) was made of polypropylene material for its ease of malleability and cost [37], the couplers of acrylonitrile butadiene (ABS) supported the stainless-steel discs (90 mm diameter), ABS to the axle stand as a shaft machined with polyvinyl chloride (PVC) material. The 12-24 V power rating was designed specifically to be enough to achieve the required rotational speeds [18]. The base of the reactor (600 x 200 mm) was made from plywood to provide a stable surface for the motor stand and electrical circuit boards.

Two UV mercury lamps producing 15 W each at a wavelength of 350 nm were positioned centrally above the rotating discs, aligned with the disc axis and centred radially, at a vertical distance of 2 cm from the disc surface and supported by aluminium reflectors covering internal walls of the RDR, promoting compactness of the reactor and reducing the losses of light to the surroundings. This configuration was selected to maximise the uniformity of irradiance across the photocatalytic surface while minimising angular incidence losses to the surface normal and shading effects between adjacent discs, thereby maximising effective photon flux according to Lambert's cosine law. Two magnetic stirrers were placed in the tank and rotated at 400 rpm to ensure sufficient mixing, which was later validated using purple dye and phenol samples as tracers, collected from different locations of the reactor and analysed with a UV-Vis spectrophotometer (Shimadzu UV-1800, 1 nm resolution). The rotation of the axle was powered by a motor controlled by a driver connected to an Arduino board, as illustrated in the electrical circuit setup (Supporting material 1). The power supply for this electrical set-up was through a Manson 0-30 V, 2.5 A, AC power supply pack [38] and the Arduino board. The latter was powered via a USB connection to the monitor input and controlled by a rotational speed code over a range of 0-255 rpm, with a set of instructions embedded in C programming [38,39].

The kinetic tests of phenol degradation were assessed by sampling 10 ml regularly taken with time from the reaction mixture through a small opening at the top of the reactor tank. The samples were replicated three times, stored in lidded tubes in a rack until they were measured using the UV-Vis spectrophotometer. The reactor design described in this section is used as proof of concept for validating the modelling studies in section 2.3.

2.3.CFD modelling

2.3.1. Fluid flow model

This section aims to investigate the distribution of local flow, the effectiveness of the photocatalyst, and the limitation of mass transfer within the immobilised catalytic layers of the rotating discs through 3D CFD modelling. The design geometry was created using the COMSOL Multiphysics geometry module and consisted of several domains and boundary conditions, as presented in Fig. 2(a). The geometry was chosen to closely match the dimensions of the experimental setup, which included three vertical discs partially immersed in a water solution. At the start of the simulation, there were two start domains for the liquid and gas phases, and two rotating domains with separate rotational speed inputs for the discs and the agitator.

The model involved a two-phase flow of air and water, with their fluid surfaces initially divided by a work plane of specified height, z. The kinetic model of phenol degradation obtained in Section 3.2 was used in the mass balance model. The turbulent k-epsilon approach was chosen to model the flow using the Equations A1.1-A1.7 in Appendix A1. Further details regarding these model parameters can be found in the cited documentation [40]. Although the liquid film formed on the rotating disc surface is expected to remain predominantly laminar because of its small thickness, the overall reactor hydrodynamics are influenced by bulk-liquid recirculation, free-surface deformation, liquid entrainment, and transient splashing generated by disc rotation. A Reynolds number estimate, based on the experimentally measured film thickness at 60 rpm (63 μm) and the peripheral disc velocity, yielded approximately 18, confirming laminar conditions within the liquid film. However, the rotating discs continuously interact with the bulk liquid and the dynamically evolving air–water interface, generating complex flow structures and enhanced momentum transport outside the thin-film region. The k–ε turbulence model was therefore adopted primarily to represent turbulent transport within the bulk liquid and near the free surface while maintaining stable coupling with the Level Set formulation and rotating-domain model.

Briefly, the momentum transport model was based on the Level set model, assuming an incompressible Newtonian liquid with constant viscosity in an isothermal environment. The conservation of mass and momentum is expressed by Equations 1 and 2, respectively.

$$\frac{\partial u}{\partial t}\,\rho + \rho(u.\nabla)u = [-pI + \mu(\nabla u + \nabla u^T) + \rho g + F_s] \qquad \text{Eq.1.}$$

$$\nabla u = 0 \qquad \text{Eq.2}$$

Where u is the velocity of water (m/s), p represents the pressure (Pa), ρ is the density (kg/m^3), u is the velocity vector (m/s), ρg and F_s are the gravitational and surface tension forces (N), respectively, and μ is the dynamic viscosity (kg/m · s). The surface tension forces distributed over the interface were calculated by the signed distance function φ to the interface of the LS approach, where σ is the surface tension coefficient and $\delta(\phi)is$ smoothed Dirac delta function at the interface.

$$F_s = \sigma\left(-\nabla \cdot \frac{\nabla\phi}{|\nabla\phi|}\right)\delta(\phi)\frac{\nabla\phi}{|\nabla\phi|} \quad Eq.3$$

This function captures the fluid interface, as shown in Eq.4 and simplifies the computation by avoiding complex curvature and normal shapes of surfaces, which are typically required in other multiphase models. [41].

$$\frac{\partial\varphi}{\partial t} + \mathrm{u}\cdot\nabla\varphi = \gamma\nabla\cdot\left(\epsilon_{ls}\nabla\varphi - \varphi(1-\varphi)\frac{\nabla\varphi}{|\nabla\varphi|}\right) \qquad \text{Eq.4.}$$

Where $\frac{\partial\varphi}{\partial t}$ is the transient derivative of external free energy (-), γ is the stabilisation parameter and the parameter ϵ_{ls} determines the thickness of the region by progressing smoothly from a value of zero to unity and is typically of the same order as the size of the elements of the mesh. The latter determined time scale, which was carefully selected to maintain a constant interfacial thickness ϵ_{ls} and avoid overdamping of the convective terms.[42] In the bulk fluid regions where there is no mixing between the fluids, one fluid was assigned $\phi = 1$, while the other was assigned $\phi = 0$. Conversely, the interface region was represented by values within the range between the two boundary values, as expressed by Equation (Eq.5.1).

$$0 \le \phi \le 1 \qquad \text{Eq.5.1}$$

The local density and dynamic viscosity of the mixture were calculated from the local volume fraction values within each cell of the calculation domain, as described by Equation (Eq. 5.2).

$\rho = \sum \alpha_q \rho_q \; ; \; \mu = \sum \alpha_q \mu_q \; ; \sum \alpha_q = 1$ q=1,2 Eq. 5.2

To solve the governing differential equations for both gas and liquid phases, initial values and boundary conditions were defined for all domains and boundaries. The initial values were specified by assuming that the liquid phase, consisting of water, filled the tank domain to a designed level in the reactor z, and that the fully dynamic mesh surrounded the rotating discs (Fig. 2(b) and Fig. 2 (c)). The gas phase, consisting of air, was located above the water phase.

2.3.2. Mass transport model

The transport of phenol included the diffusion, convection, and reaction rate models occurring within the system. The initial phenol concentration in the water phase was set to 1.55 mol/m^3. The mass transport in the water phase and on the surfaces of the discs was derived using Eqs. 5 and 6, respectively.

$\frac{\partial c_i}{\partial t} + \nabla . (-D_i \nabla c_i) + u \nabla c_i = 0$ Eq.5

$\frac{\partial c_i}{\partial t} + \nabla . (-D_{ie} \nabla c_i) = f(R_i)$ *Eq.6*

$R_i = I(I_0, \varepsilon, c_i, l) f(k_{obs}, c_i)$ *Eq.7*

Assuming the attenuation of the illumination light follows Beer's law and the reaction kinetics follow a pseudo-kinetic model, Eq. 7 is simplified in Eq.8.

$R_i = a \, I_0 e^{-\varepsilon h c_i} k_{obs}(c_i) c_i = k'_{obs}(I_0, c_i) c_i$ *Eq.8*

Where a is the surface angle of the incident light, I_0 is the incident light intensity, h is the thickness of the water film, ε is the attenuation coefficient, c_i is the concentration of phenol in water and k_{obs} is the observed pseudo-kinetic rate constant for phenol degradation. The constants D_i and D_{ie} are the molecular diffusivity in water and the effective diffusivity in the disc, respectively. The linear relation between the reaction rate and surface illumination I_0, obtained by fitting the results of the ray tracing model in section 2.3.3, is valid at high operating rotation speed of the RDR, where the degradation potential of the photocatalyst remains smaller than the surface reaction rate due to an increase in the thickness of the film covering the surface of the discs. [43]

$R_i = I_0 k'_{obs} c_i$ *Eq.9*

From prior simulation testing, it was found that the flow at the interface boundary reached a pseudo-steady state after 2.5 s of simulation time. A time constraint was introduced to account for the absence of reaction before this time, as expressed in Eq. 10.

$f(R_i) = 0$, t<2.5 s Eq.10

A sample of discretisation for solving the set of equations Eqs. 1-3 and 5-6 are shown in Fig.2(b). The meshing involved size refinements and corner trimmings. The maximum element size on the rotating domains was 0.00178 m, and the overall geometry is 0.0225 m. Identity pair boundaries were created on the rotating boundary walls of the rotating domain to allow for the movement of the meshes that includes those at the walls to move next to the static mesh walls. These boundaries consist of two layers on the same wall, enabling the wall to slide via a moving-mesh function, as highlighted in Fig. 2(c).

2.3.3. Illumination by the ray tracing model

The irradiance distribution on the surface of the discs, I_0, directly contributes to the photocatalytic activity of the coated TiO_2, as illustrated in Eq. (8). It was estimated by modelling the propagation of light from three hemispherical source lamps using a diffuse emission model. Accessing these values during dynamic LS simulations proved challenging, as the ray-tracing module requires a static interfacial geometry, whereas the LS model accounts for transient variations in the gas–liquid interface. To address this limitation, a separate static geometry model of the TiO_2-coated discs was adopted, as illustrated in Fig. 2(d). The Ray Geometry module of COMSOL Multiphysics was used

to discretise the irradiation power into photon rays illuminating the disc surfaces. The static interface used for ray tracing was extracted from the LS simulation after the gas–liquid boundary reached a stable configuration, approximately 2.5 s into computation time (see Mov 2). This corresponds to complete drainage of the initially flooded virtual domain and the establishment of a constant liquid level in the tank. After this point, the air–water interface remained effectively stationary, with temporal fluctuations in the average liquid height of less than 0.2%. The stabilised interface was therefore used as the reference geometry for the ray-tracing module. Under these steady free-surface conditions, optical interactions at the gas–liquid boundary, which include refraction, reflection, and scattering, are consistently represented. Using this stabilised interface reduced uncertainties associated with transient surface deformation and justified the use of a static ray-tracing solution as a time-averaged illumination field for coupling with the transient hydrodynamic and kinetic models. The resulting surface irradiance distribution was subsequently fitted using a three-dimensional empirical function via the COMSOL fitting module and incorporated into the kinetic model (Eq. 8).
The modelling of light propagation and incident irradiation on the catalytic surface was carried out by discretising light into rays using the Ray Optics, Geometrical Optics module of COMSOL Multiphysics v6.2. A total of 100000 rays/UV lamp were emitted from the curved boundaries of a cylindrical shape, corresponding to three equivalent lamp sources with a combined radiant power of 100 W, corresponding to the total nominal electrical power of the UV illumination system. This approach preserved the overall incident photon flux on the disc surface while simplifying the lamp geometry for numerical efficiency. The models (Eqs. 11-13) were used to define the ray propagation trajectories.[43]:

$$\frac{\mathrm{dq}}{\mathrm{dt}} = \frac{\partial \omega}{\partial \mathrm{k}} \qquad \text{Eq.11}$$

$$\frac{\mathrm{dk}}{\mathrm{dt}} = \frac{\partial \omega}{\partial \mathrm{q}} \qquad \text{Eq.11}$$

$$\omega = \frac{\mathrm{c}|\mathrm{k}|}{\mathrm{n(q)}} \qquad \text{Eq.13}$$

Where k is the wave vector, ω is the angular frequency, t is time, q is the ray position vector, n is the real part of the refractive index of the isentropic medium, and q is the position of the vector. The light was assumed to be attenuated by dispersion and reflection at the solid boundaries of the photocatalytic discs and at the internal wall of the RDR, respectively. The power of the refracted rays at the water-air boundary interface was calculated using the classical Fresnel equations [44].
The equations were solved following space discretisation in the time domain using the GMRES iterative solver Fig. 2(e). This method treated each ray as a dynamic wavefront, maintaining consistent angles within the same domain. When a ray moves from one medium to another, its wave vector is reinitialised by Snell's law.

2.3.4. Model setup

To solve the governing differential equations for the gas and water phases, initial values and boundary conditions were defined for all domains and boundaries. The initial values were specified by assuming that the water phase was present in the tank and the rotating mesh domain, whilst the gas phase was assumed to be present in the domain above the two domains. The inlet boundary was defined by the inlet velocity (u_o), and the outlet boundary by the atmospheric outlet pressure. An effective refractive index of 0.38 was assigned to water, accounting for light attenuation due to turbidity, scattering, and absorption in the wastewater matrix. [45]. Details about the model characteristics are illustrated\\ in Table 2. The transient water film flow was simulated using the COMSOL 6.2 CFD solver, considering the effects of gravity, inertia, and surface tension. The interaction of water with the solid surface was modelled using the wetted-wall boundary condition with adhesive contact and a constant static contact angle.

The LS model was initialised through a phase initialisation step using a signed distance variable (ϕ) to ensure smooth variations throughout the domain. This was followed by a transient step that solved the momentum-conservation and interface-tracking equations. Moreover, the time-dependent study

iteratively solved several nonlinear equations at each time step using Newton's method, which evaluated the Jacobian and its computationally expensive derivative. The default settings in Comsol minimised the computational power by calculating the Jacobian derivative using a constant damping factor.
The simulation started by discretising the fluid domain into many meshes, and the governing equations were then integrated for each mesh. The differential equations were computed using an iterative solver (i.e. the generalised minimal residual solver), which was coupled with the geometric multigrid preconditioner used to coarsen the mesh using a multigrid, thereby reducing the order of the shape functions. The transient simulation was conducted using a time step of 0.005 s and a convergence tolerance of 0.01%.

2.3.4. Simulation methodology

The discretisation was carried out using the built-in meshing module of Comsol, which used the Adaptive Mesh Refinement Method and generated predominantly tetrahedral domain elements and triangular surfaces. The effects of the size of these elements on the viscous forces at the surface disc boundaries were investigated using more refined meshes to assess the water film thickness. The mesh convergence check for each part of the RDR was ensured by increasing the number of mesh elements and monitoring the pressure values at three arbitrary locations from the CFD simulation. This result was subsequently confirmed by using the Grid Convergence Index (GCI) as described in Appendix A2. [46] The GCI reached values below 12%, validating the accuracy of the present numerical simulations and ensuring close independence of the mesh size.

The model was used to investigate the effects of rotational speed and fluid level on flow distribution across discs of the RDR. Several simulations were run at rotational speeds of 60, 120, and 240 rpm, with additional tests at 60 rpm at various fluid levels. The agitator's rotational speed was kept constant at 100 rpm. Each simulation was run for 5 s, resulting in a total computation time of 20 hours on a 1GB RAM server. The boundary conditions at t = 0 included an atmospheric-pressure constraint at the top of the reactor and a concentration C_0 = 1.55 mol/m^3 in the water phase. Other physical parameters were assembled in Table 2.

3. Results and Discussion

3.1. Disc surface analysis

The visible results from the sandblasting are illustrated in Fig.3. Further analysis of these surfaces conducted using the LEXT 3D microscope reveals the surface roughness observed in Fig 4a and Fig.4b. The surface profiles show a comparison before and after sandblasting where the average surface variation increased from approximately 0 µm in Fig. 4a to approximately ±5 µm in Fig. 4b. The large yellow area in Fig. 4b indicates a punch on the metal disc, marking the location of 3D measurements. This was done to ensure consistent measurements at the same location after applying dip-coatings with the TiO_2 slurry. The sandblasting process increased the surface area and improved surface contact, thereby enhancing the adhesion of the photocatalyst to the stainless-steel disc.
The observation during dip-coating discs was the visible impact of the high surface tension of the water-based TiO_2 dispersion. Upon withdrawing the discs from the TiO_2 dispersion, a thin white film formed on their surfaces during drying. This facilitated the successive deposition of homogeneous thin layers of photocatalyst. A total of 19 coating operations were performed, resulting in an average thickness of approximately 1.3 µm, estimated from catalyst weights and normalised to a disc surface area of 136 cm^2, and a photocatalyst loading of 0.55 mg/cm^2 (with disc measurements of 0.5940, 0.5926, and 0.4734 mg/cm^2). This thickness falls within the range reported in the literature, while a different glass-based substrate was used. [18].
The LEXT 3D microscope analysis of the surface roughness of disc 2 after the first, second, and fourth coatings is shown in Fig. 5. It is observed that the TiO2 profile height increased linearly with the number of dips, suggesting a similar mechanism of photocatalyst crystal deposition in each layer.

Adhesion performance was confirmed through successive rinsing with deionised water and vibration tests, with no observable loss of photocatalyst.

3.2.Reactor testing

3.2.1. Kinetics study

The designed concept was tested using TiO_2 immobilised on rotating discs, with no variation in photocatalyst loading or UV light intensity. The time-dependent degradation of phenol was used to understand the performance of the RDR in the CFD simulation studies in Section 3.3. The kinetic study was not extended to investigate model parameters such as disc rotation speed, initial phenol concentration, and incident light intensity.

When two 15 W UV light sources were used, the average light intensity across the surfaces of the discs was approximately 40 W/m². The front surface of the first disc, however, exhibited a higher light intensity of approximately 50 W/m^2 due to the increased exposure to UV light. The typical UV-Vis spectra of phenol samples, replicated three times at each time point, are illustrated in Fig. 6. The peak at 350 nm was used for quantitative analysis of phenol, as shown in Fig. 7.

The kinetic model of the main reaction of phenol decomposition into intermediate radicals and further reactions with these intermediates was simplified into a single and lumped homogeneous model of the first-order kinetics with respect to phenol and zeroth order with respect to oxygen as expressed in Eq.8. The later was justified by the sufficient solubility of oxygen and the fast diffusion rate in the water film covering the surface of the photocatalytic discs. This reduces the relevance of the rate at which the UV light captures the electrons. The kinetics of side reactions involving phenol and intermediate radicals were incorporated and lumped into the main phenol kinetic model. The system volume and concentration were set at 750 mL and 150 mg/L, respectively.

The tests were carried out over a total duration of 2 hours, showing marked phenol degradation over time, as illustrated in Fig. 8. The change in phenol concentration indicates close conversion of 9.15%, 12.3 and 13.9% after 100 min at 60, 90 rpm and 240 rpm, respectively. At a lower rotation speed of 60 rpm, the contact time between the liquid film and the disc surface was longer, thereby promoting conversion by increasing reaction time. In the provided dataset, however, phenol concentration initially decreased, followed by periods of fluctuation, which may be attributed to dynamic mass-transfer effects inherent in the present RDR. The initial reduction in concentration suggests that the degradation begins rapidly due to the availability of active photocatalytic sites and sufficient reactant concentration. The trend of the curve is thus associated with a delay in changes and fluctuations in values over a time up to 60 minutes. This period of fluctuation, which is pronounced at 60 rpm, suggests potential mass transfer limitations and poorer mixing at the surface of the photocatalyst discs and indicates a deviation of the behaviour of the model of the fluid flow from the desired behaviour of a well-stirred tank model. The fitting of the dataset to the first-order kinetic model resulted in correlations, yielding an observed kinetic constant for phenol degradation k_{obs} of 0.048 ($R^2 = 0.8376$), 0.066 h^{-1} ($R^2 = 0.9511$) and 0.084 h^{-1}($R^2 = 0.9230$) at 60, 90 and 240 rpm, respectively. These values, in terms of RDR performance, correspond to photocatalytic space-time yields (PSTY), defined herein as the mole number of pollutant degradation per reactor volume, irradiation time, and power, of 93.6, 128.3, and 144.6 mmol day^{-1} kW^{-1}, respectively.

Although direct comparison is complicated by differences in reactor geometry, irradiation source, catalyst configuration, and reaction chemistry, the obtained PSTY values can be placed in the context of previously reported photochemical and photocatalytic reactor systems. Higher PSTY values of 330.5 and 627.2 mmol day^{-1} kW^{-1} have been reported for visible-light photochemical oxidation reactions in spinning disc reactors operated under optimised residence-time and irradiation conditions [47]. Similarly, Tibbetts et al. reported a PSTY of approximately 740 mmol day^{-1} kW^{-1} for a microreactor-based photochemical oxidation process, where the high surface-area-to-volume ratio and short optical path length enhanced photon utilisation [48]. In contrast, lower PSTY values are generally reported for photocatalytic degradation systems. Yatmaz et al. achieved a PSTY of 5.49 mmol day^{-1} kW^{-1} during the photocatalytic degradation of 4-chlorophenol using immobilised TiO_2 in a spinning-disc reactor [24], while Dambruoso et al. reported values close to 10 mmol day^{-1} kW^{-1} for

singlet-oxygen-mediated sulfoxidation in a batch photoreactor [49]. These differences reflect variations in reactor geometry, irradiated area, photon flux, residence time, catalyst configuration, reaction pathway, and mass-transfer characteristics. The present results demonstrate that the photocatalytic rotating-disc reactor operates within the performance range reported for photocatalytic systems in the literature and catalyst utilisation within the RDR.

RDRs are known for enhancing mass transfer rates through shear-induced turbulence near the catalyst surface, thereby reducing the boundary layer thickness and improving reactant delivery. However, the observed variations in concentration, including minor increases at certain time intervals, could indicate competition between reaction kinetics and diffusion limitations, periodic detachment of intermediates or by-products that interfere with accurate measurement, or both. The observed degradation kinetics suggested an interplay between reaction mechanisms and mass-transfer phenomena in the RDR. It was therefore used for the CFD parametric studies on surface performance of the discs in section 3.3.

3.3. Simulation results and analysis

3.3.1. Illumination distribution

Simulations were run to determine the correlation between the distance to the irradiation source and the irradiance at the disc surface. As expected, the irradiance on the surface of the disc approached the largest values on the exposed surface of discs of normal angle to the UV lights, dropped partly at the lateral wall due to the reflective properties of walls of the reactor, assumed of mirror properties and dropped significantly at the surfaces between the discs due the geometrically limited access of UV light (Fig.9). The illuminated regions of the discs that were radially non-uniform would have their photocatalytic activity affected, whereas the discs rotate. The parts of the surfaces that were cyclically shaded (ex. the second and third discs) would have poorer photocatalytic activity.

3.3.2. Catalytic activity distribution

The first rotational speed tested was 60 rpm, with the fluid work plane level set to cover half of the disc surface (z=0). Additional fluid was also added into the rotating domain of the discs, as described in section 4.1. This addition occurred at the start of the simulation, resulting in the actual fluid level at steady state (e.g., a stable level free of splashing) being higher than the set value, as shown in Fig. 10 and further illustrated in Mov2 (supporting information). The visual representation of the water free surface in Fig.10 indicates that the level of the water phase did not stabilise until 2.5 s, as expressed in Eq. 10. The surface of the disc is analysed through visualisations of the surface shear stress, reaction rate and concentration of phenol on the discs presented in Fig.11(a), Fig.11(b) and Fig.11(c), respectively, with additional illustration in Mov3 as supporting information. The degradation of phenol is analysed through a one-dimensional (1D) plot of concentration variation over time, based on the average volume-based concentration of the solution in Fig. 12. The locations of fluid flow and low phenol concentration in Fig. 11 correlate with areas of low reaction rates. The accumulation of concentration around the circumference of the disc was influenced by a combination of rotational, surface wettability and gravity forces. Fig. 11 presents a clear concentration profile in Fig.11(c). In this figure, the water phase exhibits a high concentration, while the surface exposed to air has a much lower concentration. The clockwise rotation also reveals that phenol is dragged into the water phase, lowering its concentration, particularly on the right side of the water phase. The reaction rate is again highest around the perimeter of the disc, predominantly due to the inertial centrifugal forces. Additionally, where the fluid is dragged up, a high reaction rate is observed, explained by the initial rate of reaction being highest at the highest concentration. This distribution along the perimeter is observed to be non-symmetrical with reference to a vertical axis passing through the centre of the disc. There is more conversion at the drag-out region than the drag-in region, which suggests the relevance of the inertial rotational forces in the former region and the remaining forces, particularly the gravitational ones, in the latter region and the longer effective exposure to irradiation and

photocatalytic surface contact before re-entering the bulk liquid, resulting in enhanced cumulative conversion relative to the drag-in region.

Comparison of the irradiation distributions predicted by the ray-tracing model (Fig. 9) with the surface concentration profiles of phenol on the three discs (Fig. 11 (d)) illustrates a relationship between local photon flux and photocatalytic activity. Disc 1, which received the highest fluence rate, exhibits the most pronounced concentration depletion and the highest reaction rates, whereas progressively lower reaction rates and less phenol conversion are observed on Discs 2 and 3 as the available irradiation decreased. In general, regions exposed to higher fluence rates correspond to lower phenol concentrations due to enhanced photocatalytic degradation. However, this relationship is not linear and a direct correlation between local irradiance and local reaction rate cannot be established. As expressed in Eq. 7, the reaction rate is a function of incident irradiation, light attenuation, and local phenol concentration. Following the Beer–Lambert formulation adopted in Eq. 8, the effective photon flux reaching the photocatalyst surface depends on local film thickness and concentration, both of which vary spatially across the rotating discs. Furthermore, local photocatalytic activity is influenced by hydrodynamic factors including residence time, centrifugal transport, surface renewal, and mass-transfer limitations. The lowest phenol concentrations and highest reaction rates are therefore observed in regions where favourable irradiation conditions coincide with enhanced surface renewal and mass transfer, particularly around the upper peripheral drag-out regions of the rotating discs.

Concentration plots over time, shown in Fig. 12(a), indicate a clear decrease in concentration, with some fluctuations, after 2.5 s, once the water level has stabilised. The settled fluid emulates the setup of the experimental procedure. The rates in Eqs. 9 and 10 specify that the reaction can only occur at heights above $z = 0$ and when the volume fraction of water (α_l) exceeds 50%. The large fluctuations from 0 to 2.5 s are responses to water splashing onto the surface of the disc at heights above $z = 0$. At 2.5 s, the concentration degradation levels off, showing a more constant trend, although it continues to decrease. The conversion over the first 5 s of the reaction is calculated as 8.71%. The experimental reaction does not show large splashing effects on the disc surface, as seen in the first 2.5 s of the simulation, due to the initial setting of water in the rotating mesh domain, which required displacement of the liquid into the tank of the RDR.

As shown in Fig. 12(a), at a rotation speed of 60 rpm, the simulation results for phenol concentration align with the experimental data, The rate at the disc surface reflects both the fluid dynamics and the photocatalytic activity of the catalytic layer. Therefore, the numerical method could effectively characterise the film formation and flow dynamics. The average experimental film thickness at 60 rpm was 63 microns, close to the theoretical value of 60 microns estimated by the model of Afanasiev et al. [50] based on the physical properties of water and the capillary number. The film thickness, estimated by CFD from the water-phase volume fraction at the disc surface, was 147 microns. Because the CFD model predicted a thicker liquid film than that measured experimentally, the calculated UV attenuation is expected to be higher, resulting in a conservative estimate of the photon flux reaching the photocatalyst surface. The numerical results were assessed using the GCI, as described in Appendix A2 [46], confirming that the solution is grid-independent within the accepted uncertainty range of 12 %, but a discrepancy remains between the experimentally measured and CFD-predicted film thicknesses. This difference is not solely attributable to discretisation limits but also to inherent numerical diffusion associated with the level-set interface-tracking method, experimental uncertainty in film-thickness measurements, and the exclusion of microscale interfacial effects, such as surface roughness and capillary wave formation. Further mesh refinement, particularly near the rotating disc surface, would significantly increase computational cost without ensuring proportional improvement in predictive accuracy, given these additional modelling and measurement limitations. Importantly, the CFD model successfully reproduces the radial trends and relative variations in film thickness.

The remaining discrepancy is likely attributable to a combination of discretisation limitations, numerical diffusion inherent to the Level-Set interface-capturing approach, and unresolved surface

characteristics such as roughness and wettability. Although alternative methods, such as the Volume of Fluid (VOF) approach, may provide a sharper interface representation, they would require substantially finer meshes and significantly greater computational resources for the present transient rotating-disc simulations [51].

At 120 rpm (Fig. 12(b)), the results are similar to those at 60 rpm (Fig. 12(a). At a rotational speed of 240 rpm, however, there is a significant change in the concentration-time graph produced in Fig. 12(c). The phenol conversion after 5 s of simulation increased to 11.94%, which is confirmed by the surface distributions of reaction rate and concentrations in Fig. 13. As the rotational speed increases, more water is lifted onto the disc surface, leading to more surface renewals of phenol in the concentrated solution reacting on the exposed disc surface. The result differs from some similar findings in the literature. It has been shown that low rotation speeds, and by inference, a thinner water film, slow the water's residence time on the photocatalyst surface, thereby promoting conversion. In these cases, the limiting factor in the degradation process is the mass transfer of phenol. This indicates that, at low rotational speed, portions of the illuminated photocatalyst surface were underutilised because the transport of phenol through the liquid film was insufficient to sustain the intrinsic reaction rate. Catalyst utilisation was limited by reactant supply, although this limitation became less pronounced as rotational speed increased.

At 240 rpm, there is a greater concentration of phenol around the top perimeter of the disc, which can be attributed to the increased centrifugal forces generated at this high rotational speed. It can also be seen that the area where water is dragged onto the disc is much larger at 240 rpm, validating that more solution undergoes phenol degradation and leading to a larger conversion.

Although the CFD-predicted film thickness exceeded the experimentally measured value, the photocatalytic performance remained sensitive to operating conditions throughout the investigated range. Increasing the rotational speed from 60 to 240 rpm increased phenol conversion, indicating that the reactor remained within a mass-transfer-influenced regime. A transition to a thickness-independent or purely kinetic regime was therefore not observed. The interpretation of the results is based primarily on the relative changes in film hydrodynamics, surface renewal, and mass transfer rather than on the absolute film thickness predicted by the CFD model."

The second parameter investigated was the level of water, as it impacts wettability and, by inference, surface forces, at a constant disc rotational speed of 60 rpm. The work plane was adjusted from the original axis position z = 0 m (half-immersion of the disc) to z = -0.07 m. At this new solution level, the concentration-time graph is seen in Fig. 12(d). For this change in level to z = -0.07 m, reactivity increases compared with z = 0 m at the same rotational speed of 60 rpm. The final calculated conversion after 5 s was 17.42%, compared with the former level of 8.71% at z=0. This increase could be explained by a greater percentage of the disc surface being exposed above water, allowing reaction to occur and increasing the reaction rate. It is also observed that the initial decrease in concentration in the concentration-time figure is greater than that at z = 0 m. Further analysis of the reaction rate is shown in the surface rate and concentration profiles in Fig. 14. When comparing the disc surface at -0.07 m with the zero m level at 60 rpm, the results are similar to those observed when the rotational speed was increased from 60 to 240 rpm. Although shaft torque was not measured directly, lower immersion depths reduce the wetted area exposed to the liquid phase and are therefore expected to decrease hydrodynamic drag acting on the rotating discs. Lower immersion levels may reduce the mechanical energy required for disc rotation while increasing photocatalytic performance through greater catalyst exposure to irradiation. However, quantitative evaluation of torque and power consumption was beyond the scope of the present study. The concentration in the middle of the exposed disc is lower, while the rate of the reaction is seen to be greater around the perimeter of the disc in Fig.13, which demonstrates the relevance of the inertial centrifugal forces of the rotating discs on mass transfer limitations of phenol across the layers of water covering the discs.

Although direct torque or shaft power measurements were not performed, the relationship between mechanical energy input and reactor performance can be qualitatively inferred from hydrodynamic scaling. In rotating disc systems, mechanical energy dissipation increases with angular velocity, while mass-transfer coefficients scale linearly with the angular velocity according to classical Sherwood number correlations. Since tangential velocity increases radially, shear stress and surface renewal are greatest at the disc periphery, where photocatalytic activity was experimentally observed to be most pronounced, which indicates that rotational energy input predominantly enhances the most catalytically active region of the reactor. Furthermore, the level of liquid immersion influenced both hydrodynamic drag and energy consumption. Lower immersion depth reduced the wetted surface area and hydrodynamic resistance acting on the disc, thereby decreasing torque demand and mechanical energy input. At the same time, thin-film formation under reduced immersion promoted improved light penetration and enhanced mass transfer due to shorter diffusion distances. Consequently, partial immersion represented a favourable operating regime in which mechanical energy input was concentrated within a thin, highly active reaction zone rather than being dissipated in bulk mixing. The developed CFD approach provides a useful tool for investigating the coupled hydrodynamic, optical, and kinetic phenomena governing photocatalytic RDRs. While the laboratory-scale results demonstrate the potential of this technology, further studies at larger scales and longer operating periods are required to assess scale-up behaviour, energy efficiency, and industrial applicability.

A closer examination of the hydrodynamic and mass-transfer behaviour, interpreted using classical non-dimensional flow and transport numbers, shows that the increase in degradation rates with rotational speed and immersion level corresponds to operation within a transitional rotational Reynolds number regime. This regime is characterised by enhanced momentum transport and intensified convective mass transfer, driven by increased shear stress and radial flow along the disc surface. Moreover, a Froude number exceeding unity was reached, consistent with centrifugal effects and free-surface deformation, thereby promoting thin-film renewal and interfacial transport. These results demonstrate that reactor performance is predominantly governed by hydrodynamic scaling parameters rather than phenol-specific chemical kinetics.

4. Conclusion

This study investigated some key limitations of photocatalytic RDRs and explored strategies to improve their hydrodynamic and photocatalytic performance. While RDRs offer advantages such as enhanced surface area for light exposure, challenges remain, including limited throughput due to thin reactive films, poor mixing from laminar flow, mass-transfer limitations, and the continued reliance on UV-active photocatalysts. To improve RDR performance, strategies that enhance turbulence at lower rotational speeds remain needed, as they can reduce power consumption and minimise shear forces that may degrade photocatalysts over time.

To investigate and improve flow dynamics and mass transfer in RDRs, this study applied the LS method within a 3D modelling. This approach treated air and water as interpenetrating phases that obey conservation laws of mass and momentum. CFD simulations, validated through experimental laboratory results, provided insights into the photocatalytic reaction mechanisms occurring on disc surfaces. The custom-fabricated RDR achieved phenol degradation with a photochemical space-time yield (PSTY) of 93.6 mmol day^{-1} kW^{-1} and a catalyst loading of 0.55 mg/cm^2, a performance primarily limited by mass transfer rather than catalyst inefficiency.

To ensure uniform photocatalyst distribution without compromising the spatial performance of the discs, surface roughness analysis was conducted. Sandblasting increased the surface micro-roughness from nearly 0 μm to approximately ±5 μm, thereby improving the adhesion of the TiO_2 coating. Dip coating produced a uniform catalyst film with an average thickness of 1.3 μm and a loading of 0.55 mg/cm^2. Successive dip coatings showed a linear increase in film thickness, indicating reproducibility and controlled deposition.

Simulations assessed performance at disc speeds of 60, 120, and 240 rpm. Higher rotational speeds enhanced phenol conversion by increasing centrifugal force, gravity effects, and water film thickness. Conversion increased from 8.71% at 60 rpm to 11.42% at 240 rpm. Additionally, reducing liquid levels led to improved conversion rates, rising from 8.71% to 17.42%. These findings highlight the importance of optimising hydrodynamics for improved photocatalytic efficiency.

Performance across the disc surface was confirmed to be radially non-uniform. CFD and experimental data showed that tangential velocity and shear forces increased from the centre to the edge, leading to better mass transfer and reaction rates at the periphery. These effects facilitated catalyst regeneration. Slower speeds near the centre resulted, however, in reduced efficiency. While the developed model offers a valuable tool for assessing RDR performance, challenges remain. These include limitations in modelling the interaction between ray propagation (typically applied to static systems) and fluid dynamics in rotating geometries. To address this, ray tracing and fluid flow models were treated separately in this work.-A key contribution of this work is the development of a transient three-dimensional model that integrates free-surface hydrodynamics, UV irradiation, mass transfer, and photocatalytic surface kinetics within a rotating-disc reactor. The model enables spatially resolved analysis of film thickness, reaction rate, concentration, and shear stress distributions, revealing radial and circumferential non-uniformities in catalyst utilisation that are difficult to quantify experimentally. The results demonstrate how operating conditions influence surface renewal, mass transfer, and photocatalytic performance, providing mechanistic insight that can support reactor design and scale-up.

.

Acknowledgement

The authors would like to acknowledge the support for funding provided by the EPSRC EP/X525583/1 and the Office of Water (OFWAT)

References

[1] Ameta, R., Ameta, C.S., 2017. *Photocatalysis: Principles and Applications*. CRC Press, Miami.

[2] McCullagh, C., Skillen, N., Adams, M., Robertson, P.K.J., 2011. Photocatalytic reactors for environmental remediation: a review. *J. Chem. Technol. Biotechnol.* 86, 1002–1017.

[3] Mohd, A., 2020. Presence of phenol in wastewater effluent and its removal: an overview. *Int. J. Environ. Anal. Chem.* 6, 1362–1384.

[4] Chen, D., Ray, K.A., 1999. Photocatalytic kinetics of phenol and its derivatives over UV irradiated TiO_2. *Appl. Catal. B Environ.* 23, 143–157.

[5] Bozdek, M., Rajca, M., 2012. Photocatalysis in the treatment and disinfection of water. Part I. Theoretical backgrounds. *Ecol. Chem. Eng.* 19, 489–512.

[6] Burns, J.R., Ramshaw, C., 1996. The intensification of rapid reactions in spinning disc reactors. *Chem. Eng. Sci.* 51, 1347–1358.

[7] Meeuwse, M., de Haan, A.B., Verhoeff, H.J.J., 2010. Process intensification in a rotating packed bed. *Chem. Eng. Sci.* 65, 88–95.

[8] Ray, K., Beenackers, A.A., 1998. Development of a new photocatalytic reactor for water purification. *Catal. Today* 40, 73–83.

[9] Danckwerts, P.V., 1951. Significance of liquid-film coefficients in gas absorption. *Ind. Eng. Chem.* 43, 1460–1467.

[10] Smith, J., Brown, A., Lee, K., 2024. Enhanced photocatalytic degradation of methylene blue using a novel counter-rotating disc reactor. *Front. Chem.* 12, 1335180. https://doi.org/10.3389/fchem.2024.1335180

[11] Li, K., Zhang, H., He, Y., Tang, T., Ying, D., Wang, Y., Sun, T., Jia, J., 2015. Novel wedge structured rotating disk photocatalytic reactor for post-treatment of actual textile wastewater. *Chem. Eng. J.* 268, 10–20.

[12] Daily, J.W., Nece, R.E., 1960. Chamber dimension effects on induced flow and frictional resistance of enclosed rotating disks. *ASME J. Basic Eng.* 82, 217–232.
[13] Dorfman, L.A., 1963. *Hydrodynamic Resistance and the Heat Loss of Rotating Solids*. Oliver & Boyd.
[14] Zangeneh, H., Zinatizadeh, A., Nazari, S., Joshaghani, M., Zinadini, S., Sibali, L., Feyzi, M., 2022. Highly efficient azo dye degradation in a photocatalytic rotating disc reactor with deposited l-histidine-TiO_2-CdS. *Mater. Sci. Semicond. Process.* 105, 107071.
[15] Zhang, L., Anderson, A.W., Zhang, Z., 2006. Development and modeling of a rotating disc photocatalytic reactor for wastewater treatment. *Chem. Eng. J.* 121, 125–134.
[16] Yao, L.-B., Xu, J., Wang, H., Zhao, L., 2021. Intensification of micromixing efficiency in a spinning disk reactor: experimental investigation. *Chem. Eng. Process. Process Intensif.* 166, 108500.
[17] Boodhoo, K.V., Al-Hengari, S.R., 2012. Micromixing characteristics in a small-scale spinning disk reactor. *Chem. Eng. Technol.* 35, 1229–1237.
[18] Hamill, A.N., Weatherley, R.L., Hardacre, C., 2001. Use of a batch rotating photocatalytic contactor for the degradation of organic pollutants in wastewater. *Appl. Catal. B Environ.* 30, 49–60.
[19] Zhang, L., Kanki, T., Sano, N., Toyoda, A., 2001. Photocatalytic degradation of organic compounds in aqueous solution by a TiO_2-coated rotating-drum reactor using solar light. *Sol. Energy* 70, 331–337.
[20] Rudakova, A., Emeline, A., 2021. Photoinduced hydrophilicity of surfaces of thin films. *Colloid J.* 83, 20–48.
[21] Buechler, K.J., Nam, C.H., Zawistowski, T.M., Noble, R.D., Koval, C.A., 1999. Design and evaluation of a novel-controlled periodic illumination reactor to study photocatalysis. *Ind. Eng. Chem. Res.* 38, 1258–1263.
[22] Dionysiou, D.D., Balasubramaniam, G., Suidan, M.T., Khodadoust, A.P., Baudin, I., Laine, J.-M., 2000. Rotating disk photocatalytic reactor: development, characterization, and evaluation for the destruction of organic pollutants in water. *Water Res.* 34, 2927–2940.
[23] Damodar, R.A., Swaminathan, T., 2008. Performance evaluation of a continuous flow immobilized rotating tube photocatalytic reactor (IRTPR) immobilized with TiO_2 catalyst for azo dye degradation. *Chem. Eng. J.* 144, 59–66.
[24] Yatmaz, H., Wallis, C., Howarth, C., 2001. The spinning disc reactor – studies on a novel TiO_2 photocatalytic reactor. *Chemosphere* 42, 397–403.
[25] Negishi, N., Takeuchi, K., Ibusuki, T., 1998. Preparation of the TiO_2 thin film photocatalyst by the dip-coating process. *J. Sol-Gel Sci. Technol.* 13, 691–694.
[26] Miah, M.S., Al-Assaf, S., Yang, X., McMillan, A., 2016. Thin film flow on a vertically rotating disc of finite thickness partially immersed in a highly viscous liquid. *Chem. Eng. Sci.* 143, 226–239.
[27] Cheng, W., Wang, J., Gu, X., Feng, L., 2017. Film formation in a horizontal twin-shaft rotating disk reactor for polymer devolatilization. *Chem. Eng. Sci.* 166, 19–27.
[28] Cheng, W., Wang, J., Gu, X., Feng, L., 2018. Film flow on rotating wheel in a horizontal twin-shaft reactor for polymer devolatilization. *Chem. Eng. Sci.* 191, 468–478.
[29] Hasan, N., Aouad, W., McMillan, A.J., 2009. Determining the thickness of liquid film in laminar condition on a rotating drum surface using CFD. *Chem. Eng. Sci.* 64, 3725–3735.
[30] Yencham, J., Phan, A.N., Mens, W., Putivisutisak, S., Assabumrungrat, S., 2026. Spinning disc reactors: recent advances in CFD modeling for optimization and scale-up. *Curr. Opin. Chem. Eng.* 52, 101261.
[31] Bilger, C., Aboukhedr, M., Vogiatzaki, K., Cant, R.S., 2017. Evaluation of two-phase flow solvers using Level Set and Volume of Fluid methods. *J. Comput. Phys.* 345, 665–686.
[32] Mosleh, S., Ghaedi, M., 2021. Photocatalytic reactors: technological status, opportunities, and challenges for development and industrial upscaling, in: *Interface Science and Technology*, vol. 32, pp. 761–790.
[33] Qi, J., Ye, Y., Wu, J.J., Wang, T.H., Li, T.F., 2013. Dispersion and stability of titanium dioxide nanoparticles in aqueous suspension: effects of ultrasonication and concentration. *Water Sci. Technol.* 67, 147–151.

[34] Faustini, M., Ceratti, R.D., Boufot, M., Albouy, P.-A., Boissière, C., Grosso, D., 2014. Engineering functionality gradients by dip coating process in acceleration mode. *ACS Appl. Mater. Interfaces* 6, 17102–17110.
[35] Sathish, M., Radhika, N., Saleh, B., 2021. A critical review on functionally graded coatings: methods, properties, and challenges. *Compos. Part B Eng.* 225, 109278.
[36] Barati, N., Sani, F.M., Ghasemi, H., Sadeghian, Z., Mirhoseini, S., 2009. Preparation of uniform TiO_2 nanostructure film on 316L stainless steel by sol–gel dip coating. *Appl. Surf. Sci.* 255, 8328–8333.
[37] Chen, Y., Dionysiou, D.D., 2006. TiO_2 photocatalytic films on stainless steel: the role of Degussa P-25 in modified sol–gel methods. *Appl. Catal. B Environ.* 62, 255–264.
[38] Manson, 2024. Triple output linear mode EP-603. Available at: https://www.manson.com.hk/product/ep-603/ (accessed 20 February 2024).
[39] Arduino, 2024. Arduino - DC Motor. Available at: https://arduinogetstarted.com/tutorials/arduino-dc-motor (accessed 20 February 2024).
[40] Lou, W., Zhu, M., 2013. Numerical simulation of gas and liquid two-phase flow in gas-stirred systems based on Euler–Euler approach. *Metall. Mater. Trans. B* 44, 1251–1263.
[41] Propp, R.M., Colella, P., Crutchfield, W.Y., Day, M.S., 2000. A numerical model for trickle bed reactors. *J. Comput. Phys.* 165, 311–334.
[42] Jacqmin, D., 1999. Calculation of two-phase Navier–Stokes flows using phase-field modelling. *J. Comput. Phys.* 127, 96–127.
[43] Tong, K., Yang, L., Du, X., 2020. Modelling of TiO_2-based packing bed photocatalytic reactor with Raschig rings for phenol degradation by coupled CFD and DEM. *Chem. Eng. J.* 400, 125988.
[44] COMSOL AB, 2017. *COMSOL Multiphysics® v. 5.2, Ray Optics User's Guide*. COMSOL AB, Stockholm.
[45] Bolton, J.R., Stefan, M.I., 2002. *Fundamentals of Ultraviolet Disinfection*. American Water Works Association (AWWA), Denver, CO.
[46] Celik, I.B., Ghia, U., Roache, P.J., Freitas, C.J., Coleman, H., Raad, P.E., 2008. Procedure for estimation and reporting of uncertainty due to discretisation in CFD applications. *J. Fluids Eng.* 130, 078001.
[47] Fernández, P.A., Emanuelsson, E.A.C., 2023. Scale-up of visible light organo-photocatalytic synthesis reactions in a spinning disc reactor. *Chem. Eng. Process.* 192, 109487.
[48] Tibbetts, J.D., Carbery, D.R., Emanuelsson, E.A.C., 2017. An in-depth study of the use of eosin Y for the solar photocatalytic oxidative coupling of benzylic amines. *ACS Sustain. Chem. Eng.* 5, 9826–9835.
[49] Dambruoso, P., Ballestri, M., Ferroni, C., Guerrini, A., Sotgiu, G., Varchi, G., Massi, A., 2015. TPPS supported on core-shell PMMA nanoparticles: the development of continuous-flow membrane-mediated electrocoagulation as a photocatalyst processing method in aqueous media. *Green Chem.* 17, 1907–1917.
[50] Afanasiev, K., Münch, A., Wagner, B., 2008. Thin film dynamics on a vertically rotating disk partially immersed in a liquid bath. *Appl. Math. Model.* 32, 1894–1911.
[51] Abdelraouf, M., Rennie, A., Burns, N., Geekie, L., Najdanovic, V., Aiouache, F., 2021. Tuning the wettability of wire mesh column: pore-scale flow analysis. *Chem. Eng. J. Adv.* 8, 100181.

APPENDIX A1

The turbulent flows are therefore modelled using the Equations 5-11 where u is the velocity field vector.

$$\rho(\mathrm{u}\cdot\nabla)\mathrm{u} = \nabla\cdot[-p\mathrm{I}+\mathrm{K}]+\mathrm{F}+\rho\mathrm{g} \quad \text{(Eq. A1)}$$

$$\rho\nabla\cdot\mathrm{u} = 0 \quad \text{(Eq. A2)}$$

$$\mathrm{K} = (\mu+\mu_T)(\nabla\mathrm{u}+(\nabla\mathrm{u})^2) \quad \text{(Eq. A3)}$$

$$\rho(\mathrm{u}\cdot\nabla)k = \nabla\cdot\left[\left(\mu+\frac{\mu_T}{\sigma_k}\right)\nabla k\right]+P_k-\rho\epsilon \quad \text{(Eq. A4)}$$

$$\rho(\mathrm{u}\cdot\nabla)\epsilon = \nabla\cdot\left[\left(\mu+\frac{\mu_T}{\sigma_\epsilon}\right)\nabla\epsilon\right] + C_{\epsilon 1}\frac{\epsilon}{k}P_k - C_{\epsilon 2}\rho\frac{\epsilon^2}{k} \quad \text{(Eq. A5)}$$

$$\mu_T = \rho C_\mu \frac{k^2}{\epsilon} \quad \text{(Eq. A6)}$$

$$P_k = \mu_T[\nabla\mathrm{u}:(\nabla\mathrm{u}+(\nabla\mathrm{u})^2] \quad \text{(Eq. A7)}$$

APPENDIX A2

Potential errors associated with the CFD simulation were examined using the approach outlined by Celik et al. [38], ensuring that the results were free of mesh-size effects. The representative grid size h_0 procedure was defined as:

$$h_0 = \left(\frac{1}{N}\sum_{i=1}^{N}\Delta V_i\right)^{\frac{1}{3}} \quad \text{(Eq A2.1)}$$

where ΔV is the cell volume, and N is the number of cells. Three grid-refinement factors greater than 1.3 were used for the final refinements. The apparent order *m* of the method was defined by Equations (Eq A2.2) to (Eq A2.4.) :

$$m = \frac{\left|ln\left|\frac{\Theta_{32}}{\Theta_{21}}\right|+q(m)\right|}{ln(r_{21})} \quad \text{(Eq A2.2)}$$

$$q(m) = ln\left(\frac{r_{21}^m - s}{r_{32}^m - s}\right) \quad \text{(Eq A2.3)}$$

$$s = 1.sgn\left(\frac{\Theta_{32}}{\Theta_{21}}\right) \quad \text{(Eq A2.4)}$$

where $h_{0,1}<h_{0,2}<h_{0,3}$, $r_{21}=h_{0,2}/h_{0,1}$, $r_{32}=h_{0,3}/h_{0,2}$, $\Theta_{32}=u_3-u_2$, $\Theta_{21}=u_2-u_1$. u_k(k=1, 2, 3) expresses velocity values taken at three grid locations in the RDR and sgn is the function signum. Equation (A2.3) was solved numerically for *m*. This was used to find the relative errors (Eqs. A2.5 and A2.6) and the fine grid convergence GCI (Eqs. A2.7 and A2.8)

$$e_a^{21} = \frac{u_1 - u_2}{u_1} \quad \text{(Eq A2.5)}$$

$$e_a^{32} = \frac{u_2 - u_3}{u_2} \quad \text{(Eq A2.6)}$$

$$GCI^{21} = \frac{1.25e_a^{21}}{r_{21}^m - 1} \quad \text{(Eq A2.7)}$$

$$GCI^{32} = \frac{1.25e_a^{32}}{r_{32}^m - 1} \quad \text{(Eq A2.8)}$$

Tables and Figures

(a)

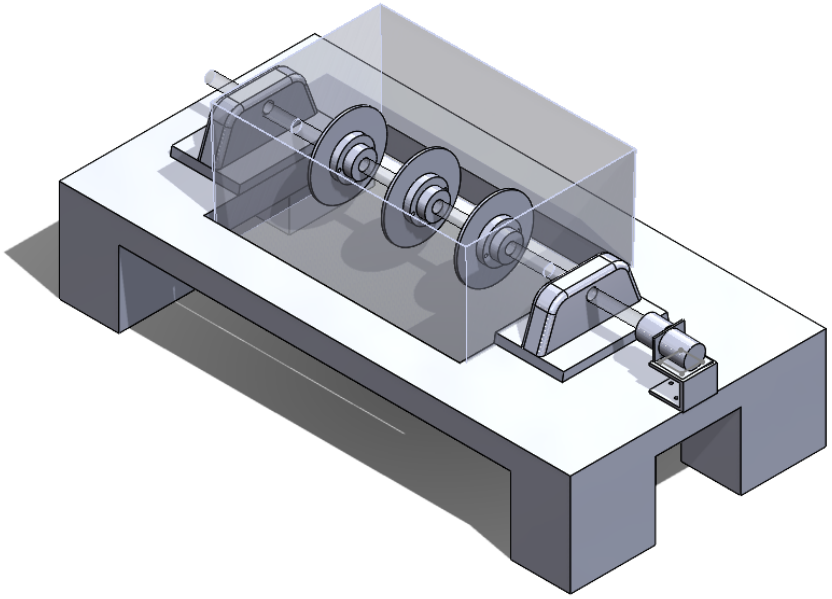

(b)

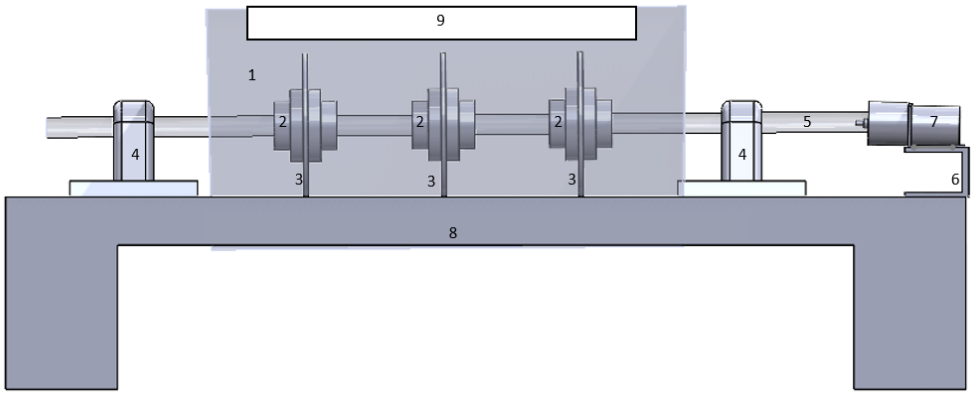

Fig. 1 Assembly parts of the batch scale rotating disc reactor design (a) 3D model and (b) 2D schematic of the batch scale rotating disc reactor design

Table 1 – List of reactor components and corresponding materials

Reactor Component	Quantity	Diagram number	Material	Dimensions (mm)
Disc	3	3	Stainless steel	90
Axle	1	5	PVC	12.6
Axle stand	2	4	ABS	-
Ball bearings	2	-	Stainless steel	12.5 mm
Coupler	6	2	ABS	-
Base	1	8	Plywood	600 x 300 mm
Reactor tank	1	1	PET	300 x 200 mm
UV lamp	2	9	Glass bulb	300 mm
Nuts & bolts	20	-	Steel	M3.5
Screws	11	-	Brass	M4

Table 2 Parameters of LS and optical geometry models

Multiphase model	Level set
Fluid	Air-water
Contact angle	60^0
Surface tension N/m)	0.0729
Operating pressure (atm)	1
Operating pressure (K)	293
Inlet pressure (Pa)	1000
Bulb power (W)	15
Internal transmittance at 10 mm thickness in air (%)	99.5
Wavelength (nm)	350
Refractive index of water	0.38
Internal transmittance at 10 mm thickness in water (%)	-
Total reflection at the top wall and no reflection by the lateral walls of the RDR	-

(a) (b)

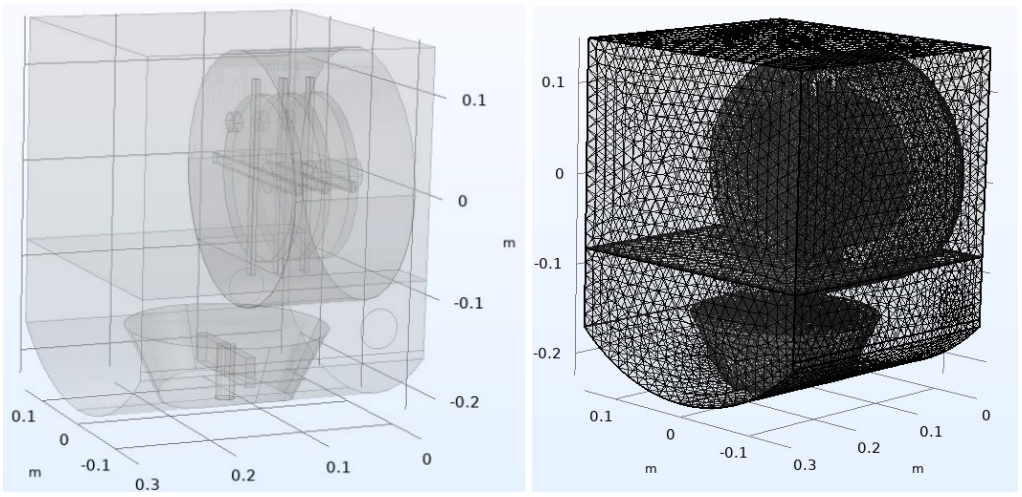

(c)

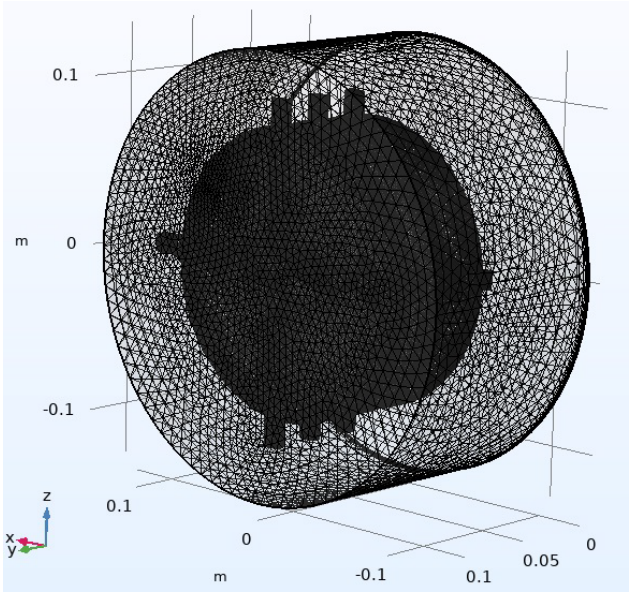

(d) (e)

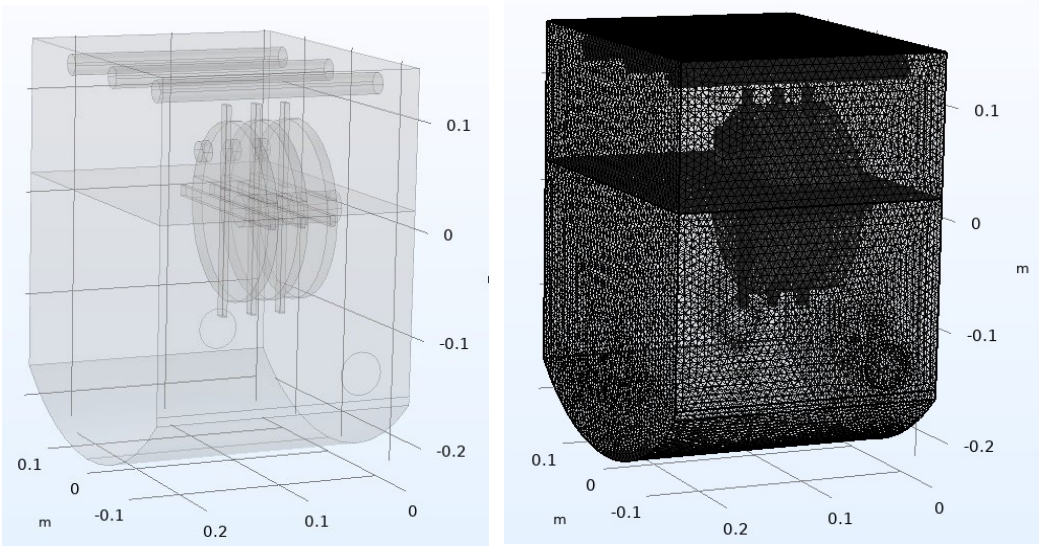

Fig. 2 Three-dimensional reactor model of the dynamic and static structures of the RDR: (a) Dynamic geometry structure, (b) Model discretisation approach of dynamic structure (c) Identity pair boundary domains of dynamic structure. (d) Geometry structure of the static structure with illumination, (e) Model discretisation approach of the static structure with illumination

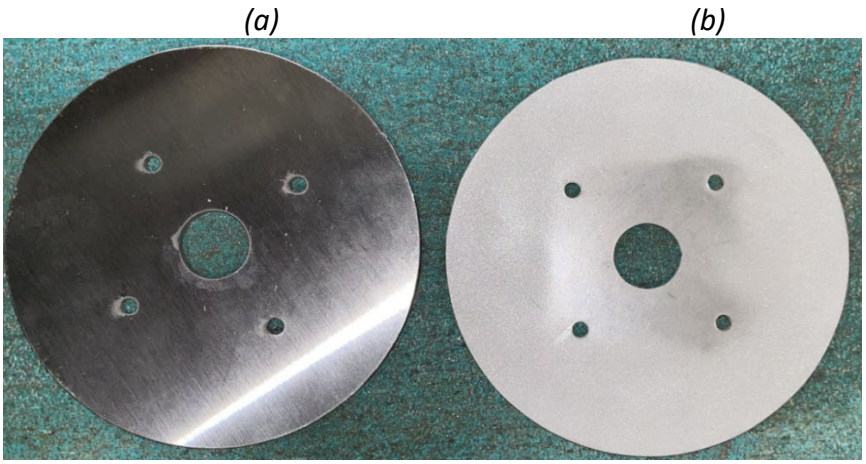

Fig.3 Sand blasting at 10 bar for 20 s exposure per unit area: (a) before and (b)after operation

(a)

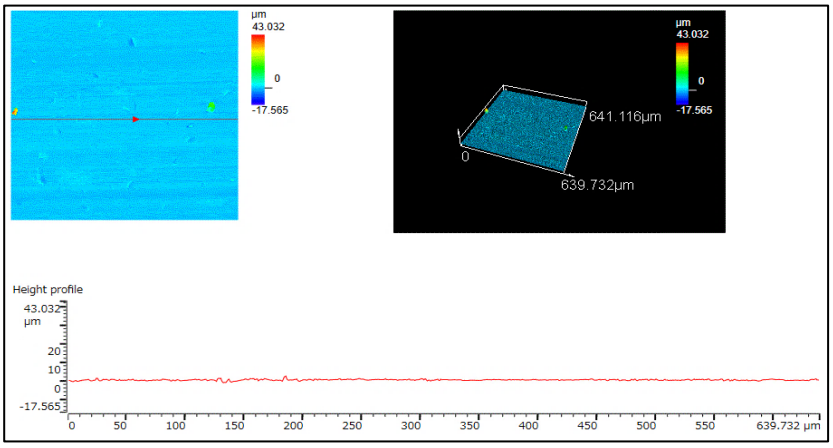

(b)

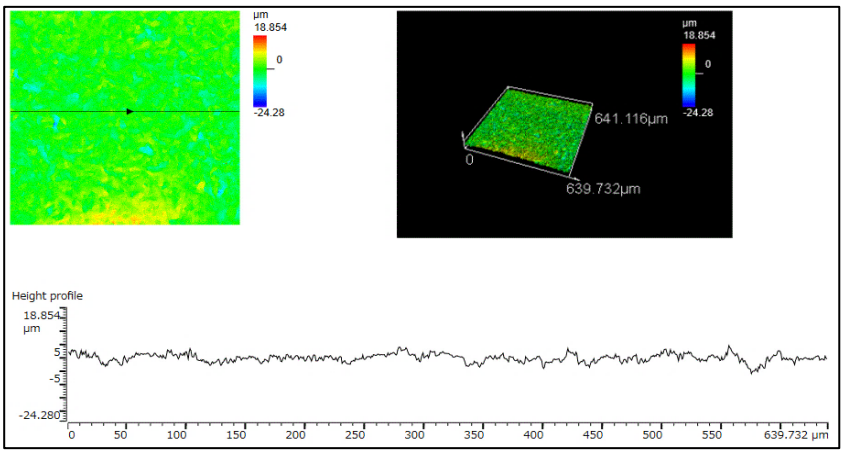

Fig.4 LEXT 3D microscopy reports of the stainless-steel disc surface showing scan images and height profile across the scan a) original untreated disc, b) 20s exposure sandblasted disc

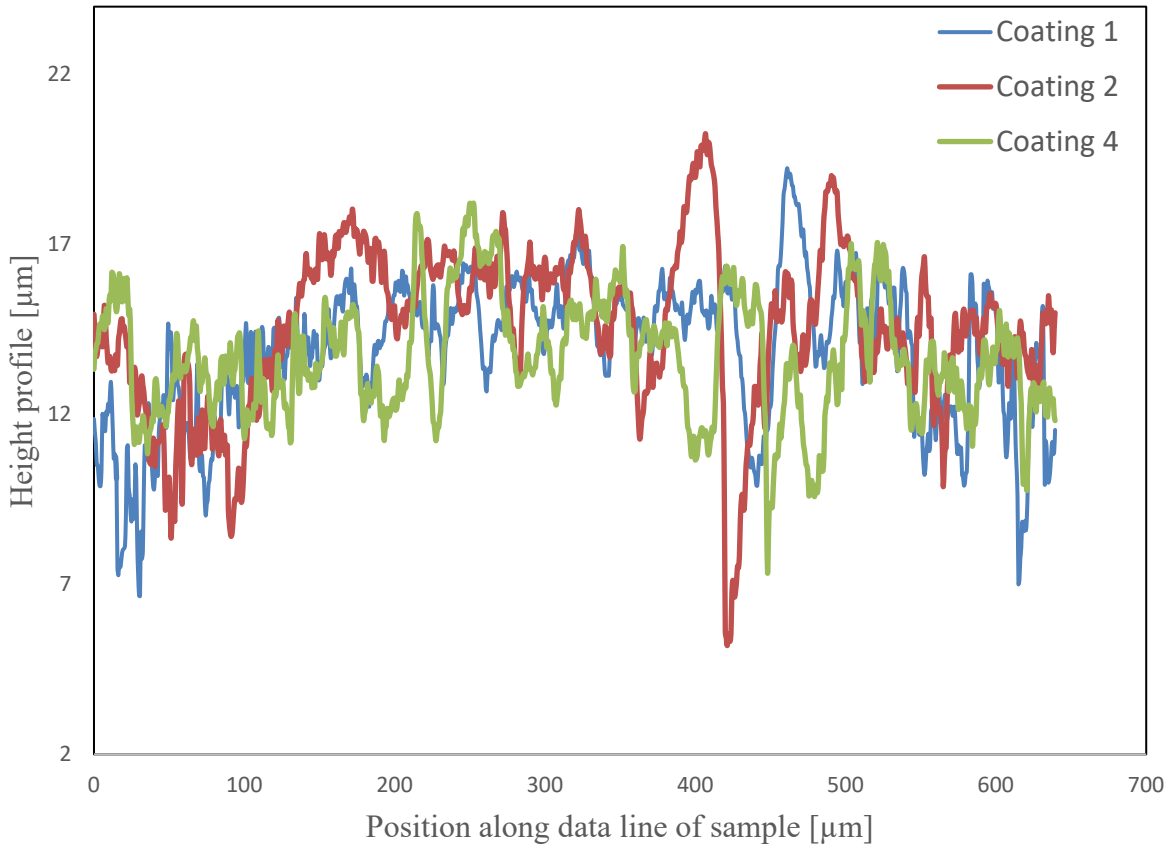

Fig.5 - Surface profile along horizontal section of Disc 2 after (blue line) one coating (average height profile: 13.87 µm), (Orange line) two coatings 9 average height profile: 14.55 µm) and (Green line) after four coatings (average height profile: 13.68 µm)

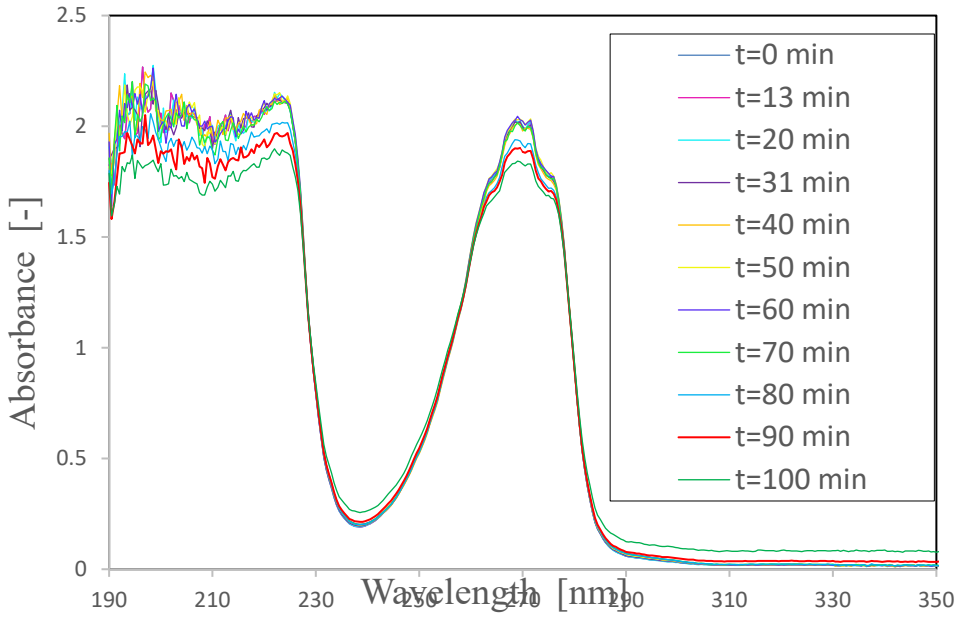

Fig. 6 - Absorbance spectra for samples over 0-100 minutes

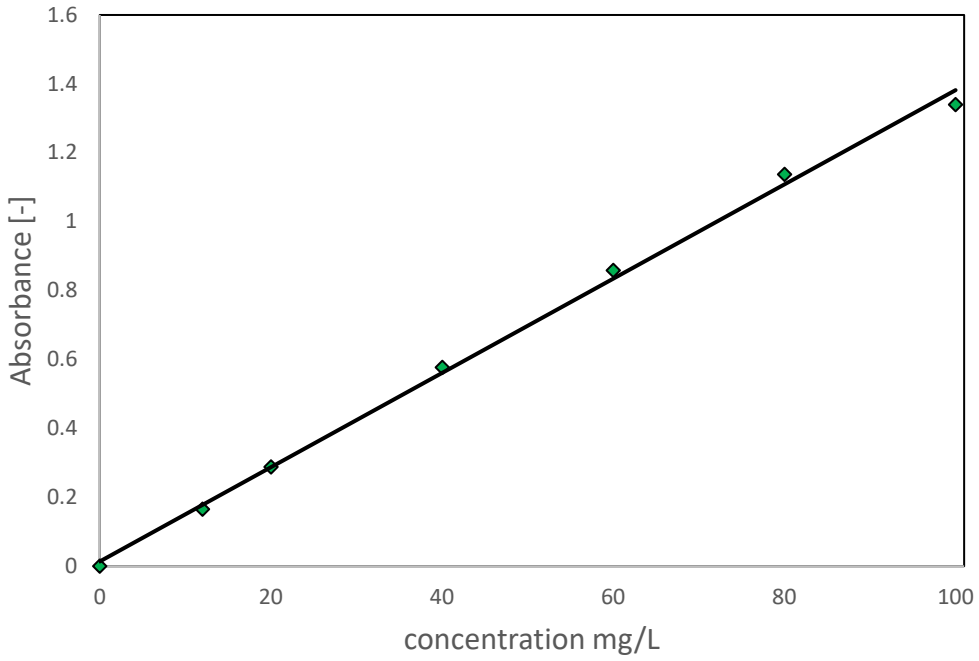

Fig. 7 – Concentration of phenol calibration curve by UV-Vis absorbance

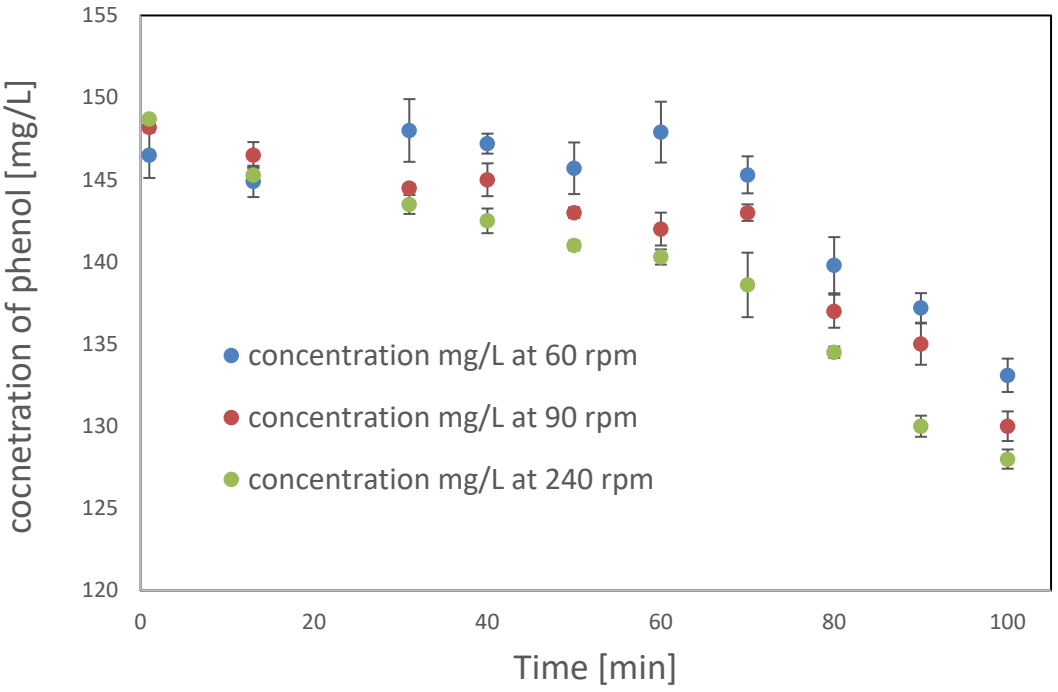

Fig.8 - Concentration vs time for phenol degradation from 0 to 100 minutes. Initial concentration 150 mg/L, Two illumination bulbs of 15 W.

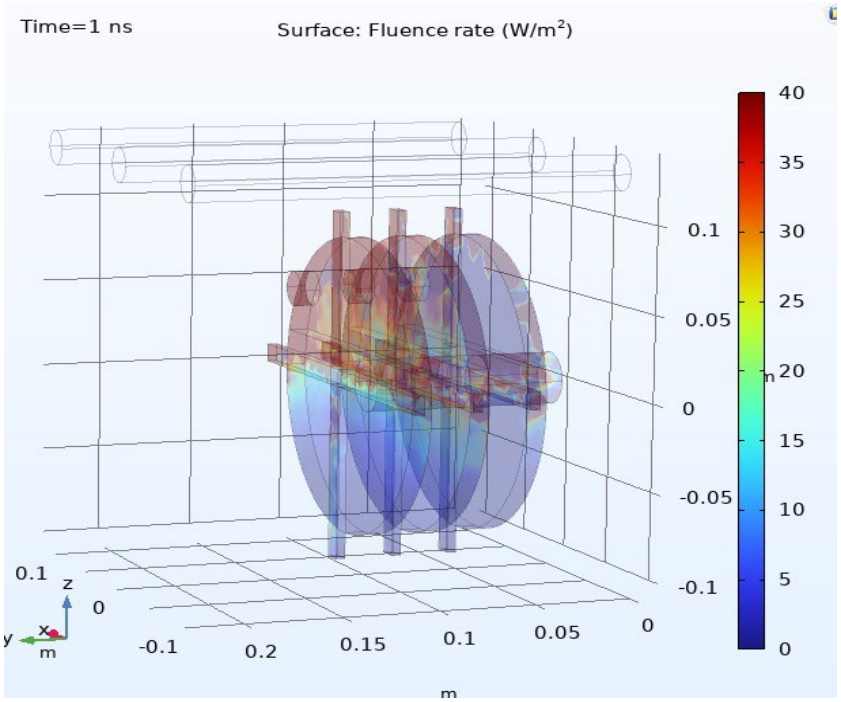

Fig 9- Surface illumination of discs of the RDR. Three bulbs of 15 W each

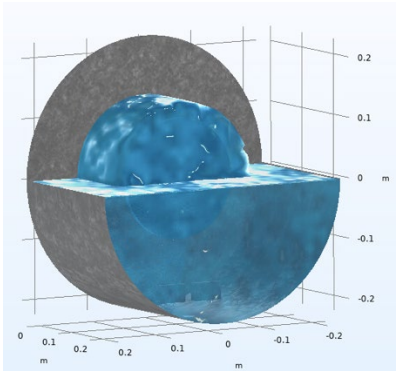

Water free surface, 0 s

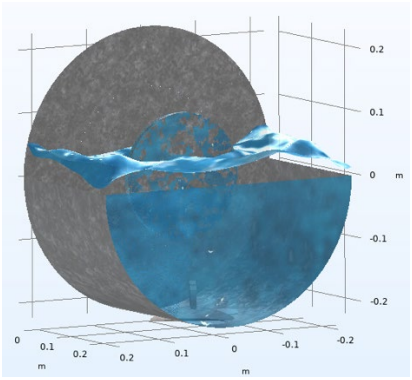

Water free surface, 1 s

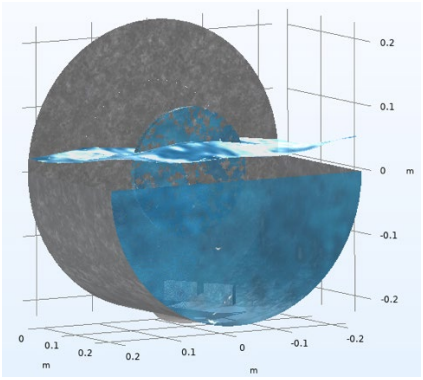

Water-free surface, 2 s

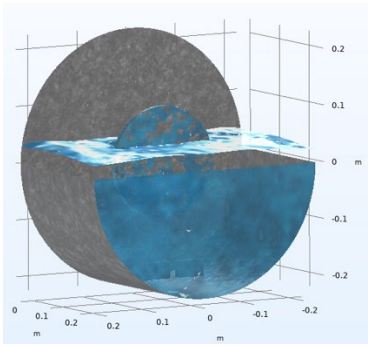

Water-free surface, 3 s

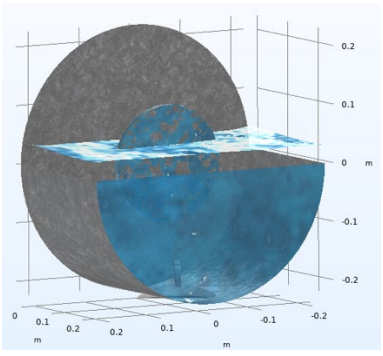

Water-free surface, 4 s

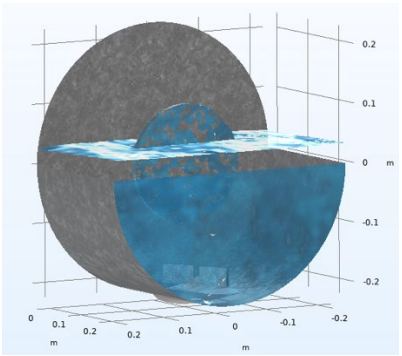

Water-free surface, 5 s

Fig. 10 - Water free surface model visualisation for 0-5 seconds simulation time at 60 rpm disc rotation at z = 0 m.

(a) (b)

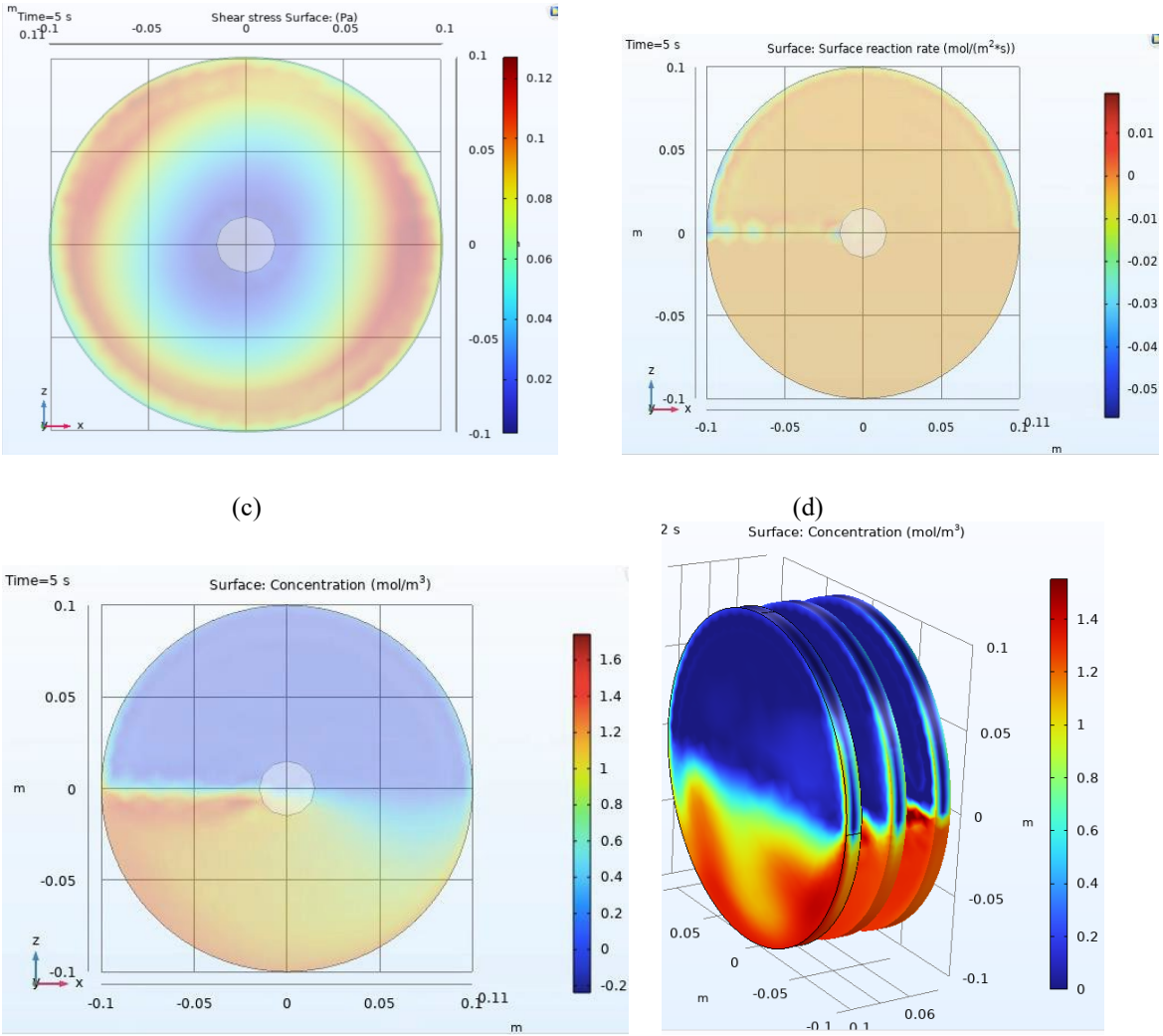

Fig.11 – (a) Surface shear stress, (b) Surface reaction rate, (c) Surface concentration, and (d) surface concentration visualisations of the three discs on plain walls at 5 s of simulation for 60 rpm disc rotation at z = 0 m

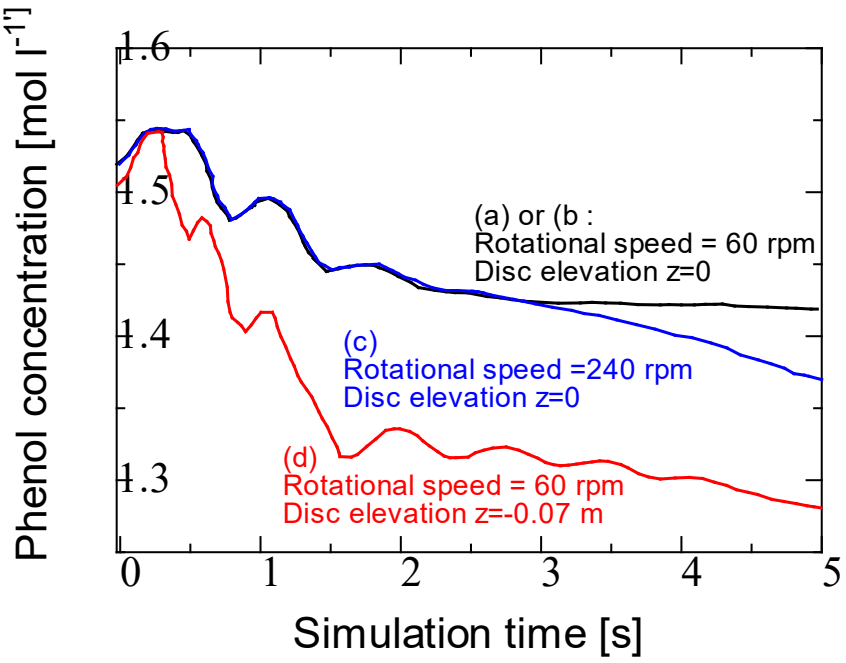

Fig.12 - Concentration-time graph for (a) 60 rpm and elevation z=0, (b) 120 r pm and elevation z=0, (c) 120 rpm and elevation z= 0 and (d) 60 rpm and elevation z=-0.07 m

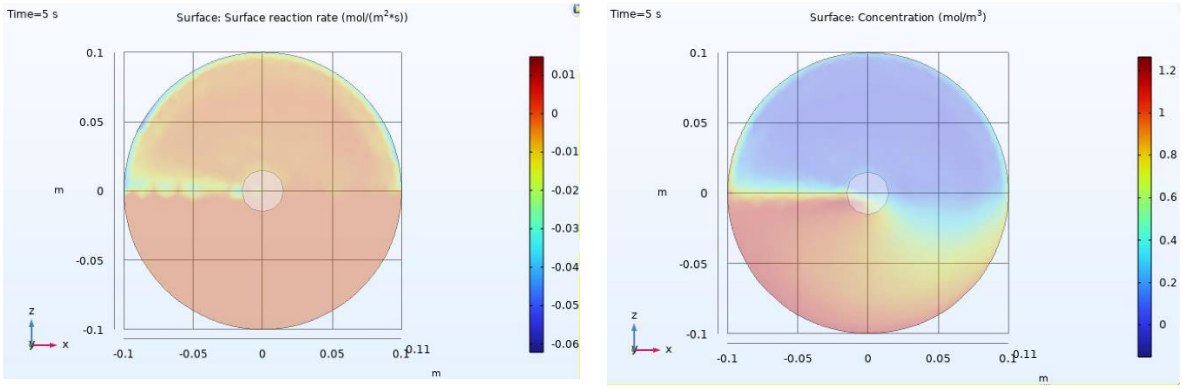

Fig.13 - Visualisation at 5 s of simulation for 240 rpm disc rotation at z = 0 m Left: Surface reaction rate, Right: Surface concentration

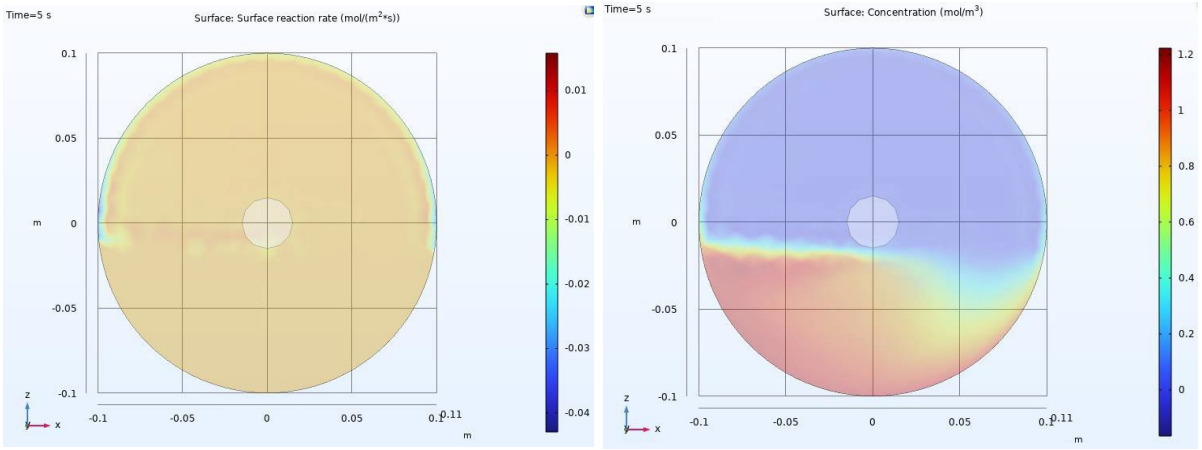

Fig.14 – Visualisation at 5 s of simulation for 60 rpm disc rotation at z = -0.07 m, Left: Surface reaction rate, Right: Surface concentration of phenol